Verification of a Many-Ion Simulator of the Dicke Model Through Slow Quenches across a Phase Transition

A. Safavi-Naini,[1,2] R. J. Lewis-Swan,[1,2] J. G. Bohnet,[3] M. Gärttner,[1,2,4] K. A. Gilmore,[3] J. E. Jordan,[3]
J. Cohn,[5] J. K. Freericks,[5] A. M. Rey,[1,2] and J. J. Bollinger[3]

[1]*JILA, NIST and University of Colorado, 440 UCB, Boulder, Colorado 80309, USA*
[2]*Center for Theory of Quantum Matter, University of Colorado, Boulder, Colorado 80309, USA*
[3]*NIST, Boulder, Colorado 80305, USA*
[4]*Kirchhoff-Institut für Physik, Universität Heidelberg, Im Neuenheimer Feld 227, 69120 Heidelberg, Germany*
[5]*Department of Physics, Georgetown University, Washington, DC 20057, USA*

We use a self-assembled two-dimensional Coulomb crystal of ∼70 ions in the presence of an external transverse field to engineer a simulator of the Dicke Hamiltonian, an iconic model in quantum optics which features a quantum phase transition between a superradiant (ferromagnetic) and a normal (paramagnetic) phase. We experimentally implement slow quenches across the quantum critical point and benchmark the dynamics and the performance of the simulator through extensive theory-experiment comparisons which show excellent agreement. The implementation of the Dicke model in fully controllable trapped ion arrays can open a path for the generation of highly entangled states useful for enhanced metrology and the observation of scrambling and quantum chaos in a many-body system.

Introduction.—Quantum many-body systems featuring controllable coupled spin and bosonic degrees of freedom (d.o.f.) are becoming a powerful platform for the realization of quantum simulators with easily tunable parameters. These include, for example, cavity QED (CQED) systems [1–8] and trapped-ion arrays [9,10]. Most often, these systems have been operated in the far detuned regime where the bosons do not play an active role in the many-body dynamics and, instead, are used to mediate spin-spin coupling between particles. Great progress has been realized in this effective spin-model regime including the implementation of long range Ising models with and without an external transverse field and the exploration of rich physics with them such as entanglement dynamics [1,2,11–17], many-body localization [18], time crystals [19], and dynamical phase transitions [20,21]. On the other hand, excluding few particle implementations [22–30], the regime where the bosonic d.o.f. actively participate in the many-body dynamics has remained largely unexplored.

In this work, we focus on this regime and report the implementation of a simulator of the Dicke model, an iconic model in cavity QED which describes the coupling of a (large) spin and an oscillator, in a self-assembled two-dimensional (2D) crystal of ions. The Dicke model is of broad interest as it exhibits rich physics including quantum phase transitions and nonergodic behavior [31]. More recently, it has gained renewed attention due to the implementation of the closely related Tavis-Cummings model in circuit QED [32] and its realization in CQED experiments with cold bosonic atoms [6–8,33,34]. In the

latter, the Dicke model emerged as an effective Hamiltonian when one encodes a two-level system in two different momentum states of a Bose-Einstein condensate (BEC) coupled by the cavity field. Within this framework, the normal to superradiant transition maps to a transition between a standard zero momentum BEC and a quantum phase with macroscopic occupation of the higher-order momentum mode and the cavity mode.

While CQED experiments have used the intracavity light intensity and time of flight images to monitor the phase transition, here, instead, we probe the two distinct quantum phases of the Dicke model by using various controlled ramping protocols of a transverse field across the critical point (see Fig. 1). We benchmark the dynamics by experimentally measuring full distribution functions of the spin d.o.f. and then comparing them with theoretical calculations. The spin observables also allow us to infer the development of spin-phonon correlations.

Our implementation of the Dicke model and corresponding observation of the phase transition in a trapped ion setup represents a complementary work with respect to the CQED platform and illustrates the power and universal nature of quantum simulation. It also opens a path for using the high level control and tunability of trapped ion experiments for the generation of highly entangled states suitable to quantum metrology in the near term future, and for the exploration of regimes currently intractable to theory.

Spin-boson system.—Our experimental system is comprised of a 2D single-plane array of laser-cooled $^9\mathrm{Be}^+$ ions in a Penning trap. The internal states forming the spin-1/2

system are the valence electron spin states in the Be$^+$ ion ground state which, in the 4.46 T magnetic field, are split by 124 GHz [16,17,36,37]. The interplay of the Coulomb repulsion and the electromagnetic confining potentials supports a set of normal vibrational modes of the crystal [38], which we couple to the spin d.o.f. via a spin-dependent optical dipole force (ODF), generated by the interference of a pair of lasers with beat note frequency ω_R [36]. The frequency ω_R is detuned from the center-of-mass (c.m.) mode frequency, $\omega_{\text{c.m.}}$, by $\delta \equiv \omega_R - \omega_{\text{c.m.}}$ (Fig. 1). The detuning is chosen to predominantly excite the c.m. mode which uniformly couples all the ions in the crystal [16]. In the presence of an additional transverse field,
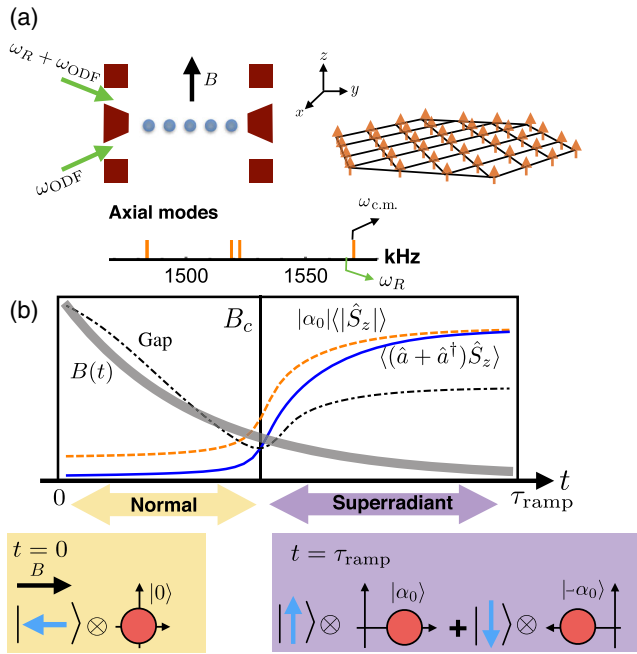

FIG. 1. Implementation and dynamical protocol. (a) The Dicke model is engineered with a Penning trap ion crystal of $N \sim 70$ ions by applying an optical dipole force, resonant only with the center of mass mode (which generates spin-phonon interactions) and resonant microwaves (which generate the transverse field). The system is initially prepared in the normal phase where all the spins point along the transverse field and are decoupled from the phonons. (b) As the transverse field is slowly turned off [using linear or exponential ramp (shown here) profiles with ramp time τ_{ramp}] the infinite system enters the superradiant phase after crossing the quantum critical point at $B(t_{\text{crit}}) = B_c$ where the gap closes. The superradiant phase with macroscopic phonon population, ferromagnetically aligned spins and large spin-phonon entanglement is described by the order parameter $\langle(\hat{a} + \hat{a}^\dagger)\hat{S}_z\rangle$, which is tracked closely by the rescaled spin observable $|\alpha_0|\langle|\hat{S}_z|\rangle$. (c) In the perfectly adiabatic regime, the ground state evolves from a separable spin-paramagnetic and vacuum photon Fock state into a macroscopic spin-phonon cat state: a superposition of two opposite spin aligned and displaced-coherent phonon states (with the sign of the superposition dictated by a parity symmetry, see Supplemental Material [35]).

generated by resonant microwaves, we implement the Dicke Hamiltonian [39–41]

$$\hat{H}^{\text{Dicke}}/\hbar = -\frac{g_0}{\sqrt{N}}(\hat{a} + \hat{a}^\dagger)\hat{S}_z + B(t)\hat{S}_x - \delta\hat{a}^\dagger\hat{a}. \quad (1)$$

in the frame rotating with ω_R. The operator $\hat{a}(\hat{a}^\dagger)$ is the bosonic annihilation (creation) operator for the c.m. mode, $B(t)$ is the time-varying strength of the applied transverse field, and g_0 represents the homogeneous coupling between each ion and the c.m. mode. Here, $\delta < 0$. We have introduced the collective spin operators $\hat{S}_\alpha = (1/2)\sum_j \hat{\sigma}_j^\alpha$ where $\hat{\sigma}_j^\alpha$ is the corresponding Pauli matrix for $\alpha = x, y, z$ which acts on the jth ion.

The Dicke Hamiltonian exhibits a quantum phase transition at $B_c = g_0^2/|\delta|$ in the thermodynamic limit, i.e., $N \rightarrow \infty$, [42–44], separating the normal ($B > B_c$) and superradiant ($B < B_c$) phases. The Hamiltonian remains unchanged under the simultaneous transformations $\hat{S}_x \rightarrow \hat{S}_x$, $\hat{S}_z \rightarrow -\hat{S}_z$, $\hat{S}_y \rightarrow -\hat{S}_y$, and $\hat{a} \rightarrow -\hat{a}$. These are generated by the parity operator $\hat{\Pi} = e^{i\pi[\hat{a}^\dagger\hat{a}+\hat{S}_x+(N/2)]}$.

In the strong-field regime of the normal phase, $B \gg B_c$, the spins and phonons decouple into a product state. When $|B| > |\delta|$ the corresponding ground state, $|\psi_{0,N/2}^{\text{Nor}}\rangle$, and low lying excitations, $|\psi_{n=1,2,...}^{\text{Nor}}\rangle$, are $|\psi_{n,N/2}^{\text{Nor}}\rangle = |n\rangle \otimes |-N/2\rangle_x$. We use $|n\rangle$ to denote Fock states and $|M\rangle_{\alpha=\{x,y,z\}}$ to denote the fully symmetric ($S = N/2$) eigenstates which satisfy $\hat{S}_\alpha|M\rangle_\alpha = M|M\rangle_\alpha$ with $-N/2 \leq M \leq N/2$.

In the weak-field limit, $B \ll B_c$, of the superradiant phase, the spin and phonon d.o.f. are entangled and the ground state becomes degenerate in the thermodynamic limit. For a finite system, it approaches $|\psi_{0,N/2}^S\rangle = (1/\sqrt{2})(|\alpha_0, 0\rangle \otimes |N/2\rangle_z \pm |-\alpha_0, 0\rangle \otimes |-N/2\rangle_z)$ as $B \rightarrow 0$, where we have introduced the displaced Fock states $|\alpha, n\rangle \equiv \hat{D}(\alpha)|n\rangle$ with $\hat{D}(\alpha) = e^{\alpha\hat{a}^\dagger-\alpha^*\hat{a}}$ the associated displacement operator [45]. Here, the sign of the superposition is dictated by the parity symmetry: for even N, the ground state will be the symmetric superposition with $\langle e^{i\pi[\hat{a}^\dagger\hat{a}+\hat{S}_x+(N/2)]}\rangle = 1$, while for odd N, the ground state is the antisymmetric superposition with $\langle e^{i\pi[\hat{a}^\dagger\hat{a}+\hat{S}_x+(N/2)]}\rangle = -1$. In this weak-field regime, the spins exhibit ferromagnetic order, characterized by the nonzero value of the order parameter $|\hat{S}_z|$, while the phonon mode acquires a macroscopic expectation value equal to $|\alpha_0|^2$, where $\alpha_0 = g_0\sqrt{N}/(2\delta)$. The low-lying excitations correspond to displaced Fock states, $|\psi_{n>0,N/2}^S\rangle$, if $\delta^2 < g_0^2$ and to spin-flips along $\hat{z}$, $|\psi_{0,M<N/2}^S\rangle$, if $\delta^2 > g_0^2$.

Slow quench dynamics.—At the start of the experimental sequence (see Fig. 1), we prepare the initial spin state $|-N/2\rangle_x$ with the aid of a resonant microwave pulse. Doppler-limited cooling of the phonon d.o.f. leads to an initial transverse phonon thermal state with mean
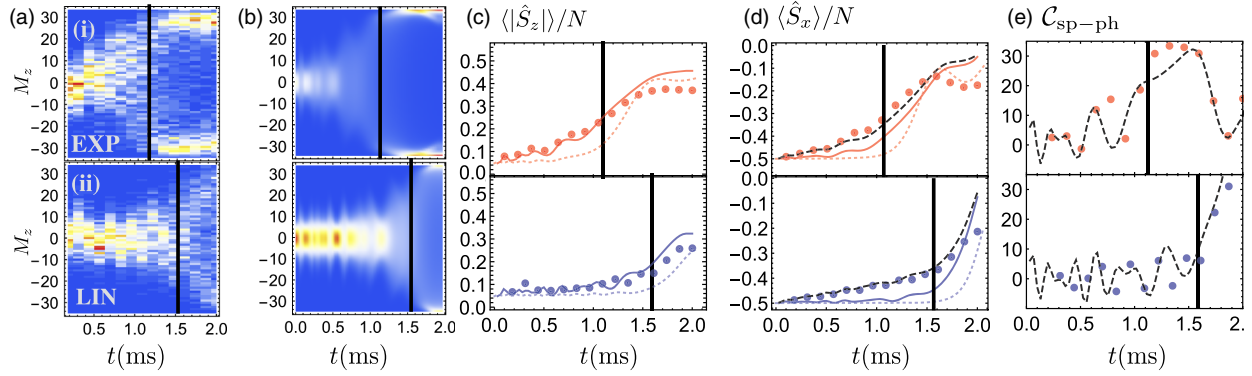
FIG. 2.   Benchmarking the simulator: Column (a) shows the experimentally measured distribution function along z, and (b) the corresponding theoretical simulations neglecting decoherence. Column (c) shows the corresponding mean values of the magnetization $\langle|\hat{S}_z|\rangle$, (d) spin projection $\langle\hat{S}_x\rangle$, and (e) $\mathcal{C}_{\mathrm{sp-ph}} \equiv \langle(\hat{a} + \hat{a}^\dagger)\hat{S}_y\rangle$. The filled circles are experimental measurements (statistical error is on the order of marker size), the colored solid and black dashed lines are the theory results without and with dephasing [the latter curve is absent in panel (c) as the z magnetization is less sensitive to this dominant source of decoherence] and the colored dotted lines are the Lipkin model results. We indicate the time at which B_c is reached in each ramp by a vertical line. The initial field is $B(t=0)/(2\pi) \approx 7.1$ kHz, $g_0/(2\pi) \approx 1.32$ kHz, $\delta/(2\pi) = -1$ kHz, and $J/(2\pi) = 1.75$ kHz. Respective ion numbers are $N = 68$ [EXP —row (i)] and $N = 69$ [LIN—row (ii)].

occupation $\bar{n} \sim 6$. For these parameters, the system starts in the normal phase close to the ground state. The transverse field is then quenched to zero (while the spin-phonon coupling and detuning are held constant) according to two different profiles: (i) Linear (LIN): $B(t) = B_0(1 - t/\tau_{\mathrm{ramp}})$, and (ii) Exponential (EXP): $B(t) = B_0 e^{-t/\tau}$. We set $\tau_{\mathrm{ramp}} = 2$ ms and $\tau \approx 600$ μs.

To characterize the performance of the simulator and the entrance into the superradiant phase, we experimentally measure the full spin distribution along the z direction (Fig. 2) by determining the global ion fluorescence scattered from the Doppler cooling laser on the cycling transition for ions in $|\uparrow\rangle_z$ [16,17,36,37]. For repeated experimental trials, we infer the state populations, $N_\uparrow$ and $N_\downarrow$ and calculate the spin-projection $M_z \equiv N_\uparrow - N/2$ for each experimental shot by counting the total number of photons collected on a photomultiplier tube in a detection period, typically 5 ms. Off-resonant light scattering from the ODF lasers is our main source of decoherence dominated by single-particle dephasing at a rate Γ_{el} [46].

As noted above, the experimental implementation and corresponding numerical simulations were carried out with $N \approx 70$ atoms. However, a well-defined crossover between the normal and superradiant phases, signaled by a well-defined minimum in the energy gap between the ground and excited states of the same parity sector [see Fig. 1(b)], appears for crystals larger than $N \gtrsim 5$ (see Supplemental Material [35]).

Our theory-experiment comparisons are based on numerical solutions of the Dicke model dynamics combined with thermal averaging. If decoherence is neglected, the spin d.o.f. is constrained to the $S = N/2$ manifold. In this reduced Hilbert space, we can exactly treat the quantum dynamics. While for the non-negligible thermal

phonon occupation in this experiment, a classical treatment of the dynamics is sufficient to reproduce the measured observables, a complete formulation of the quantum dynamics becomes necessary for colder conditions, when thermal fluctuations are insufficient to drive dynamics, and instead, quantum correlations must be properly accounted for. We observe good qualitative agreement between the experimental spin probability distribution and the theoretically computed unitary dynamics as shown in Figs. 2(a) and 2(b). In particular, both show a clear transition to a bimodal structure as the field strength is ramped down through B_c (indicated by the black vertical line in each plot), with some "smearing" due to the thermal occupation of the phonons.

To quantitatively determine the performance of the simulator, we plot the evolution of the effective order parameter $\langle|\hat{S}_z|\rangle/N$ (experimental values are extracted from the measured distribution) in Fig. 2(c), which clearly builds up as one crosses B_c. The transition is not abrupt, and instead, exhibits small amplitude oscillations, most clearly evident in the theoretical calculations, which reflect the active role of the phonons given our initial finite thermal phonon occupation. In particular, our numerical simulations show a dependence of the oscillation amplitude on the initial phonon occupation (see Supplemental Material [35]). However, the frequency of the phonon oscillations is difficult to determine and interpret, as it depends on the complex interplay between the magnitude of the initial phonon occupation and the changing transverse field. We contrast this behavior with the case when the phonons can be adiabatically eliminated and realize an effective spin Lipkin model (LM), $\hat{H}^{\mathrm{LM}}/\hbar = (J/N)\hat{S}_z^2 + B(t)\hat{S}_x$ where $J = g_0^2/\delta$. The Lipkin model dynamics features a sharper increase in magnetization after the critical

point, and significant disagreement with the experimental observations.

To further benchmark the simulator, we carry out similar measurements of the spin distribution along the x direction, extracted by applying a global $\pi/2$ pulse before the fluorescence measurement. Figure 2(d) shows the mean-value of the spin projection $\langle \hat{S}_x \rangle$. We observe x depolarization as the system exits the normal phase. The Lipkin model dynamics also exhibits a sharper depolarization across B_c than the one seen in the experiment. In this case, however, we do observe deviations between the experiment and the ideal theory. The reason is that, unlike the z magnetization, this observable is strongly affected by dephasing. Since treating the full spin-boson system in the presence of decoherence is computationally challenging, we model the effect of dephasing as $\langle \hat{S}_x \rangle \rightarrow \langle \hat{S}_x \rangle e^{-\Gamma t}$ and $\langle \hat{S}_z \rangle \rightarrow \langle \hat{S}_z \rangle$ where $\Gamma = \Gamma_{el}/2$, which is asymptotically valid in the $B \gg B_c$ and $B \ll B_c$ limits [47]. We can determine Γ_{el} experimentally when $B = 0$, and we find $\Gamma_{el} \approx 120 \text{ s}^{-1}$. However, at large B, most clearly evidenced in the LIN protocol, the demagnetization is faster than this estimate and is consistent with $\Gamma_{el} = 280 \text{ s}^{-1}$ [48]. For both ramps, we observe excellent agreement to the experiment when dephasing is accounted for.

Although measuring the phonon population might be possible following the protocol reported in Ref. [49], instead, we infer the buildup of spin-phonon correlations from the time evolution of the spin observable $\langle \hat{S}_x \rangle$. Specifically, we assume the dynamics of the system are captured by the Lindblad master equation for the density matrix of the spin-phonon system $\hat{\rho}$,

$$\frac{d\hat{\rho}}{dt} = -\frac{i}{\hbar}[\hat{H}^{\text{Dicke}}, \hat{\rho}] + \frac{\Gamma_{el}}{2}\sum_{i=1}^{N}(\hat{\sigma}_i^z \hat{\rho} \hat{\sigma}_i^z - \hat{\rho}), \qquad (2)$$

where single-particle dephasing is taken to be the dominant decoherence mechanism. From the master equation, we derive the equation of motion $(d/dt)\langle \hat{S}_x \rangle$, and rearrange to obtain the relation (see Supplemental Material [35])

$$\mathcal{C}_{\text{sp-ph}} \equiv \langle (\hat{a} + \hat{a}^\dagger)\hat{S}_y \rangle \equiv \frac{\sqrt{N}}{g_0}\left(\Gamma_{el}\langle \hat{S}_x \rangle + \frac{d}{dt}\langle \hat{S}_x \rangle\right). \qquad (3)$$

We extract the spin-phonon correlation from the experimental data by evaluating the rhs of the above expression, and calculating the time-derivative numerically with a one-sided derivative. The results are plotted in Fig. 2(e). We use the same value of Γ_{el} as in Fig. 2(d). The results are compared with a theoretical calculation of $\mathcal{C}_{\text{sp-ph}}$ [again modeling dephasing using $\langle \hat{S}_x \rangle_\Gamma \equiv \langle \hat{S}_x \rangle_{\Gamma=0} e^{-\Gamma t}$]. In principle, the correlator vanishes when evaluated for the ground state at any field strength. However, for these slow quenches, it acquires a finite value, which, in particular, grows in the superradiant phase due to population of

excited states. This is attributable due to diabatic excitations created during the ramping protocol or the initial thermal phonon ensemble. Thus, while the correlation $\mathcal{C}_{\text{sp-ph}}$ shows similar dynamical features observed in the other observables, it gives an alternative insight into the excitations created during the ramp.

While we have used the two ramp profiles to benchmark the experiment, we note that the EXP ramp has more utility in preparing a final state close to the expected ground state $|\psi_{0,N/2}^S\rangle$ in the superradiant phase. For instance, the EXP ramp produces a clearer bimodal structure in the spin probability distribution along z, and the associated larger mean absolute spin projection $\langle |\hat{S}_z| \rangle$. Future experiments could improve assessment of the adiabaticity of the quench protocols by measuring any coherences present between the different spin components, as discussed below.

Accounting for spin-phonon entanglement will be key to properly diagnosing the generated many-body quantum state. For example, tracing out the phonons from $|\psi_{0,N/2}^S\rangle$ will exponentially suppress the coherence between the spin states $|\pm N/2\rangle_z$ (see Supplemental Material [35]). To benchmark the performance of the adiabatic dynamics, it is then highly desirable to, first, perform a protocol to disentangle the spins and phonons and, only after that, characterize the state by independently measuring the spins and the phonons without information loss.

To disentangle spin and phonons, we propose to instantaneously quench the detuning $\delta \rightarrow \delta' = 2\delta$ at the end of the ramp ($B \rightarrow 0$) and, then, let the system evolve for a time $t_d = \pi/\delta'$. At t_d, the phonons are coherently displaced by $-g_0\sqrt{N}/(2|\delta|)\langle S_z \rangle$ back to the origin, while the spins only acquire an irrelevant global phase [41]. The resulting disentangled state ideally becomes $(1/\sqrt{2})[|+\alpha_0,0\rangle|+N/2\rangle_z + |-\alpha_0,0\rangle|-N/2\rangle_z] \rightarrow (1/\sqrt{2})|0\rangle \otimes [|+N/2\rangle_z + |-N/2\rangle_z]$ which has maximal spin coherence.

Summary and discussion.—We have reported the experimental realization of a simulator of the Dicke model with a 2D ion crystal of ~ 70 ions and verified its dynamics through extensive theory-experiment comparisons. Our trapped-ion simulator provides a complementary approach to related realizations in cold atoms [6–8], which is a key step in benchmarking quantum simulators which go beyond the capacity of classical computation. Our realization of a many-ion simulator of the Dicke model also paves the way for future investigation of dynamical phase transitions [20,21], quantum chaos, and fast scrambling via out-of-time order correlation measurements [17,50–53]. Moreover, the tunability of the trapped-ion setup opens the possibility of investigating more general spin-boson models [54], in particular, by operating beyond the uniform coupling regime or the preparation of states outside the fully symmetric Dicke manifold.

The slow quench protocols demonstrated above present a path to generate highly entangled states useful for quantum

enhanced metrology [55,56]. Cat states are a useful metrological resource as they are composed of a coherent superposition of states that are macroscopically displaced in phase space, leading to quantum-enhanced phase sensitivity up to the Heisenberg limit [57,58]. In particular, the spin-boson cat state $|\psi_{0,N/2}^{S}\rangle$ would be a metrological resource for sensing collective spin rotations [57], motional rotation [24,59], and coherent displacements for force sensing applications [60]. This could be achieved by using smaller systems (e.g., $N \sim 20$), reducing the initial thermal population of the phonon mode, and shifting the detuning δ away from B_c, which increases the minimum energy gap at the critical point, and consequently, the characteristic timescale to remain adiabatic (see Supplemental Material [35]). We expect this regime will be accessible in the near term future in part due to the successful implementation of electromagnetic induced transparency cooling [61].

[1] I. D. Leroux, M. H. Schleier-Smith, and V. Vuletić, Phys. Rev. Lett. 104, 073602 (2010).

[2] O. Hosten, R. Krishnakumar, N. J. Engelsen, and M. A. Kasevich, Science 352, 1552 (2016).

[3] H. Ritsch, P. Domokos, F. Brennecke, and T. Esslinger, Rev. Mod. Phys. 85, 553 (2013).

[4] K. Baumann, C. Guerlin, F. Brennecke, and T. Esslinger, Nature (London) 464, 1301 (2010).

[5] F. Brennecke, T. Donner, S. Ritter, T. Bourdel, M. Köhl, and T. Esslinger, Nature (London) 450, 268 (2007).

[6] K. Baumann, C. Guerlin, F. Brennecke, and T. Esslinger, Nature (London) 464, 1301 (2010).

[7] K. Baumann, R. Mottl, F. Brennecke, and T. Esslinger, Phys. Rev. Lett. 107, 140402 (2011).

[8] J. Klinder, H. Keler, M. Wolke, L. Mathey, and A. Hemmerich, Proc. Natl. Acad. Sci. U.S.A. 112, 3290 (2015).

[9] D. Porras and J. I. Cirac, Phys. Rev. Lett. 92, 207901 (2004).

[10] K. Kim, M.-S. Chang, R. Islam, S. Korenblit, L.-M. Duan, and C. Monroe, Phys. Rev. Lett. 103, 120502 (2009).

[11] R. Blatt and C. F. Roos, Nat. Phys. 8, 277 (2012).

[12] P. Jurcevic, B. P. Lanyon, P. Hauke, C. Hempel, P. Zoller, R. Blatt, and C. F. Roos, Nature (London) 511, 202 (2014).

[13] C. Senko, P. Richerme, J. Smith, A. Lee, I. Cohen, A. Retzker, and C. Monroe, Phys. Rev. X 5, 021026 (2015).

[14] P. Richerme, Z.-X. Gong, A. Lee, C. Senko, J. Smith, M. Foss-Feig, S. Michalakis, A. V. Gorshkov, and C. Monroe, Nature (London) 511, 198 (2014).

[15] R. Islam, E. E. Edwards, K. Kim, S. Korenblit, C. Noh, H. Carmichael, G.-D. Lin, L.-M. Duan, C.-C. J. Wang, J. K. Freericks, and C. Monroe, Nat. Commun. 2, 377 (2011).

[16] J. G. Bohnet, B. C. Sawyer, J. W. Britton, M. L. Wall, A. M. Rey, M. Foss-Feig, and J. J. Bollinger, Science 352, 1297 (2016).

[17] M. Gärttner, J. G. Bohnet, A. Safavi-Naini, M. L. Wall, J. J. Bollinger, and A. M. Rey, Nat. Phys. 13, 781 (2017).

[18] J. Smith, A. Lee, P. Richerme, B. Neyenhuis, P. W. Hess, P. Hauke, M. Heyl, D. A. Huse, and C. Monroe, Nat. Phys. 12, 907 (2016).

[19] J. Zhang, P. W. Hess, A. Kyprianidis, P. Becker, A. Lee, J. Smith, G. Pagano, I. D. Potirniche, A. C. Potter, A. Vishwanath, N. Y. Yao, and C. Monroe, Nature (London) 543, 217 (2017).

[20] P. Jurcevic, H. Shen, P. Hauke, C. Maier, T. Brydges, C. Hempel, B. P. Lanyon, M. Heyl, R. Blatt, and C. F. Roos, Phys. Rev. Lett. 119, 080501 (2017).

[21] J. Zhang, G. Pagano, P. W. Hess, A. Kyprianidis, P. Becker, H. Kaplan, A. V. Gorshkov, Z.-X. Gong, and C. Monroe, Nature (London) 551, 601 (2017).

[22] J. S. Pedernales, I. Lizuain, S. Felicetti, G. Romero, L. Lamata, and E. Solano, Sci. Rep. 5, 15472 (2015).

[23] D. Lv, S. An, Z. Liu, J.-N. Zhang, J. S. Pedernales, L. Lamata, E. Solano, and K. Kim, Phys. Rev. X 8, 021027 (2018).

[24] K. G. Johnson, J. D. Wong-Campos, B. Neyenhuis, J. Mizrahi, and C. Monroe, Nat. Commun. 8, 697 (2017).

[25] D. Kienzler, C. Flühmann, V. Negnevitsky, H.-Y. Lo, M. Marinelli, D. Nadlinger, and J. P. Home, Phys. Rev. Lett. 116, 140402 (2016).

[26] C. Monroe, D. M. Meekhof, B. E. King, and D. J. Wineland, Science 272, 1131 (1996).

[27] K. Toyoda, R. Hiji, A. Noguchi, and S. Urabe, Nature (London) 527, 74 (2015).

[28] S. Debnath, N. M. Linke, S.-T. Wang, C. Figgatt, K. A. Landsman, L.-M. Duan, and C. Monroe, Phys. Rev. Lett. 120, 073001 (2018).

[29] J. M. Raimond, M. Brune, and S. Haroche, Rev. Mod. Phys. 73, 565 (2001).

[30] I. Aedo and L. Lamata, Phys. Rev. A 97, 042317 (2018).

[31] A. Altland and F. Haake, Phys. Rev. Lett. 108, 073601 (2012).

[32] J. M. Fink, R. Bianchetti, M. Baur, M. Göppl, L. Steffen, S. Filipp, P. J. Leek, A. Blais, and A. Wallraff, Phys. Rev. Lett. 103, 083601 (2009).

[33] Z. Zhiqiang, C. Hui Lee, R. Kumar, K. J. Arnold, S. J. Masson, A. S. Parkins, and M. D. Barrett, Optica 4, 424 (2017).

[34] Z. Zhiqiang, C. Hui Lee, R. Kumar, K. J. Arnold, S. J. Masson, A. L. Grimsmo, A. S. Parkins, and M. D. Barrett, Phys. Rev. A **97**, 043858 (2018).

[35] See Supplemental Material at http://link.aps.org/supplemental/10.1103/PhysRevLett.121.040503 for details of calculation and experiment.

[36] B. C. Sawyer, J. W. Britton, A. C. Keith, C.-C. Joseph Wang, J. K. Freericks, H. Uys, M. J. Biercuk, and J. J. Bollinger, Phys. Rev. Lett. **108**, 213003 (2012).

[37] M. J. Biercuk, H. Uys, A. P. Vandevender, N. Shiga, W. M. Itano, and J. J. Bollinger, Quantum Inf. Comput. **9**, 920 (2009).

[38] C.-C. Joseph Wang, A. C. Keith, and J. K. Freericks, Phys. Rev. A **87**, 013422 (2013).

[39] R. H. Dicke, Phys. Rev. **93**, 99 (1954).

[40] B. M. Garraway, Phil. Trans. R. Soc. A **369**, 1137 (2011).

[41] M. L. Wall, A. Safavi-Naini, and A. M. Rey, Phys. Rev. A **95**, 013602 (2017).

[42] C. Emary and T. Brandes, Phys. Rev. Lett. **90**, 044101 (2003).

[43] C. Emary and T. Brandes, Phys. Rev. E **67**, 066203 (2003).

[44] P. A. Ivanov and D. Porras, Phys. Rev. A **88**, 023803 (2013).

[45] A. Wunsche, Quantum Opt. **3**, 359 (1991).

[46] H. Uys, M. J. Biercuk, A. P. VanDevender, C. Ospelkaus, D. Meiser, R. Ozeri, and J. J. Bollinger, Phys. Rev. Lett. **105**, 200401 (2010).

[47] S. F. Huelga, C. Macchiavello, T. Pellizzari, A. K. Ekert, M. B. Plenio, and J. I. Cirac, Phys. Rev. Lett. **79**, 3865 (1997).

[48] This dephasing could be a result of the experimental system going beyond the Lamb-Dicke regime, which is implicitly assumed in the derivation of the Dicke Hamiltonian, Eq. (1).

[49] K. A. Gilmore, J. G. Bohnet, B. C. Sawyer, J. W. Britton, and J. J. Bollinger, Phys. Rev. Lett. **118**, 263602 (2017).

[50] S. H. Shenker and D. Stanford, J. High Energy Phys. 03 (2014) 67.

[51] A. Kitaev, in *Proceedings of the Fundamental Physics Prize Symposium*, 2014 (unpublished).

[52] J. Maldacena, S. H. Shenker, and D. Stanford, J. High Energy Phys. 08 (2016) 106.

[53] B. Swingle, G. Bentsen, M. Schleier-Smith, and P. Hayden, Phys. Rev. A **94**, 040302 (2016).

[54] A. Shankar, J. Cooper, J. G. Bohnet, J. J. Bollinger, and M. Holland, Phys. Rev. A **95**, 033423 (2017).

[55] P. Feldmann, M. Gessner, M. Gabbrielli, C. Klempt, L. Santos, L. Pezzè, and A. Smerzi, Phys. Rev. A **97**, 032339 (2018).

[56] J. Cohn, A. Safavi-Naini, R. J. Lewis-Swan, J. G. Bohnet, M. Garttner, K. A. Gilmore, E. Jordan, J. J. Bollinger, A. M. Rey, and J. K. Freericks, New J. Phys. **20**, 055013 (2018).

[57] J. J. Bollinger, W. M. Itano, D. J. Wineland, and D. J. Heinzen, Phys. Rev. A **54**, R4649 (1996).

[58] F. Toscano, D. A. R. Dalvit, L. Davidovich, and W. H. Zurek, Phys. Rev. A **73**, 023803 (2006).

[59] W. C. Campbell and P. Hamilton, J. Phys. B **50**, 064002 (2017).

[60] M. Penasa, S. Gerlich, T. Rybarczyk, V. Métillon, M. Brune, J. M. Raimond, S. Haroche, L. Davidovich, and I. Dotsenko, Phys. Rev. A **94**, 022313 (2016).

[61] A. Safavi-Naini, R. J. Lewis-Swan, J. G. Bohnet, M. Garttner, K. A. Gilmore, E. Jordan, J. Cohn, J. K. Freericks, A. M. Rey, and J. J. Bollinger (to be published).

Supplemental Material: Verification of a many-ion simulator of the Dicke model through slow quenches across the quantum critical point

A. Safavi-Naini,[1, 2, *] R. J. Lewis-Swan,[1, 2, *] J. G. Bohnet,[3] M. Gärttner,[1, 2, 4] K. A. Gilmore,[3] J. E. Jordan,[3] J. Cohn,[5] J. K. Freericks,[5] A. M. Rey,[1, 2] and J. J. Bollinger[3]

[1]*JILA, NIST and University of Colorado, 440 UCB, Boulder, CO 80309, USA*
[2]*Center for Theory of Quantum Matter, University of Colorado, Boulder, CO 80309, USA*
[3]*NIST, Boulder, CO 80305, USA*
[4]*Kirchhoff-Institut für Physik, Universität Heidelberg,*
Im Neuenheimer Feld 227, 69120 Heidelberg, Germany
[5]*Department of Physics, Georgetown University, Washington, DC 20057, USA*
(Dated: May 7, 2018)

I. FINITE SIZE EFFECTS IN OBSERVING THE PHASE TRANSITION

The quantum phase transition of the Dicke model only truly emerges in the thermodynamic limit $N \to \infty$ [1, 2]. It is thus important to consider the relevance of finite size effects, specifically pertaining to the number of ions N and thus the collective spin length $S = N/2$.

In this spirit, we plot the order parameter $\langle (\hat{a} + \hat{a}^\dagger) \hat{S}_z \rangle$ and energy gap Δ between the ground-state and excited state in the same parity sector, for various ion numbers in Fig. 1 and as a function of transverse field strength B. A minimum in the energy gap, as a function of B, emerges for $N \gtrsim 5$. This minimum is associated with the crossover between the normal and superradiant phase, and thus we predict that features of the crossover should be observable for $N \gtrsim 5$. This is consistent with the increasingly sharp transition observable in the order parameter for $N \gtrsim 5$. Similarly, calculation of the spin observables $|S_z|$ and S_x from dynamical ramps [plotted as a function of $B(t)$, parameters taken as per Fig. 2b of the manuscript], indicate that the crossover between normal and superradiant phases is evident for $N \gtrsim 5$, which is easily satisfied by the experimentally considered crystal of $N \sim 70$.

II. EFFECT OF THE RESONANCE ON THE ENERGY GAP

As discussed in the main text, the Dicke Hamiltonian features a spin-boson resonance at $B = |\delta|$. At this field strength, the states $|m\rangle |-N/2\rangle_x$ and $|m-k\rangle |-N/2+k\rangle_x$, with k a positive integer, become nearly degenerate and can be resonantly coupled. The location of this resonance, relative to the critical field strength B_c, can greatly affect the energy spectrum of the Dicke model and in particular the magnitude of the energy gap Δ between the ground-state and excited states in the same parity sector. In this context, we can separate the effects

of the resonance into two cases, defined by the relative position of the resonance to the critical field strength:

- Case (i): $|\delta| \gg B_c$. In this regime the resonance $B \simeq |\delta|$ is well separated from the critical point. The ground-state $|\psi_{0,N/2}^{\mathrm{Nor}}\rangle = |0\rangle |-N/2\rangle_x$ is decoupled from other states at resonance. Thus, the dynamics can be affected by resonant couplings to other states (as above) only if excited states have become occupied throughout the quench.

- Case (ii): $|\delta| \sim B_c$. If the resonance is in the proximity of the quantum critical point then the low-lying excitations near the critical point of the Dicke Hamiltonian are non-trivial superpositions of spin and phonon excitations. A radical consequence of this complex interplay is the relative reduction of the energy gap between the ground and the first excited states of the same parity at the critical point. We illustrate this in Fig. 2 as a function of detuning δ, with the spin-phonon coupling g_0 scaled such that the critical field strength $B_c = g_0^2/\delta$ is held fixed.

III. ADDITIONAL SEQUENCE TO DISENTANGLE THE SPIN CAT-STATE

In the main text, we briefly outline a procedure to disentangle the pure spin-cat state from adiabatic preparation of the ground-state of the Dicke Hamiltonian. Here, we expand upon this discussion and give the appropriate details to verify this step.

In the weak-field limit, $B \ll B_c$, the ground-state of the Dicke Hamiltonian is the spin-phonon cat-state:

$$|\psi_{0,N/2}^S\rangle = \frac{1}{\sqrt{2}} \Big(|\alpha_0, 0\rangle |N/2\rangle_z \pm |-\alpha_0, 0\rangle |-N/2\rangle_z \Big), \ (1)$$

where $\alpha_0 = g_0\sqrt{N}/(2\delta)$. Without loss of generality we fix the sign of the superposition due to conservation of the spin-phonon parity symmetry, which dictates that the positive superposition is prepared by an adiabatic quench from the strong-field ground-state $|\psi_{0,N/2}^{\mathrm{Nor}}\rangle$.

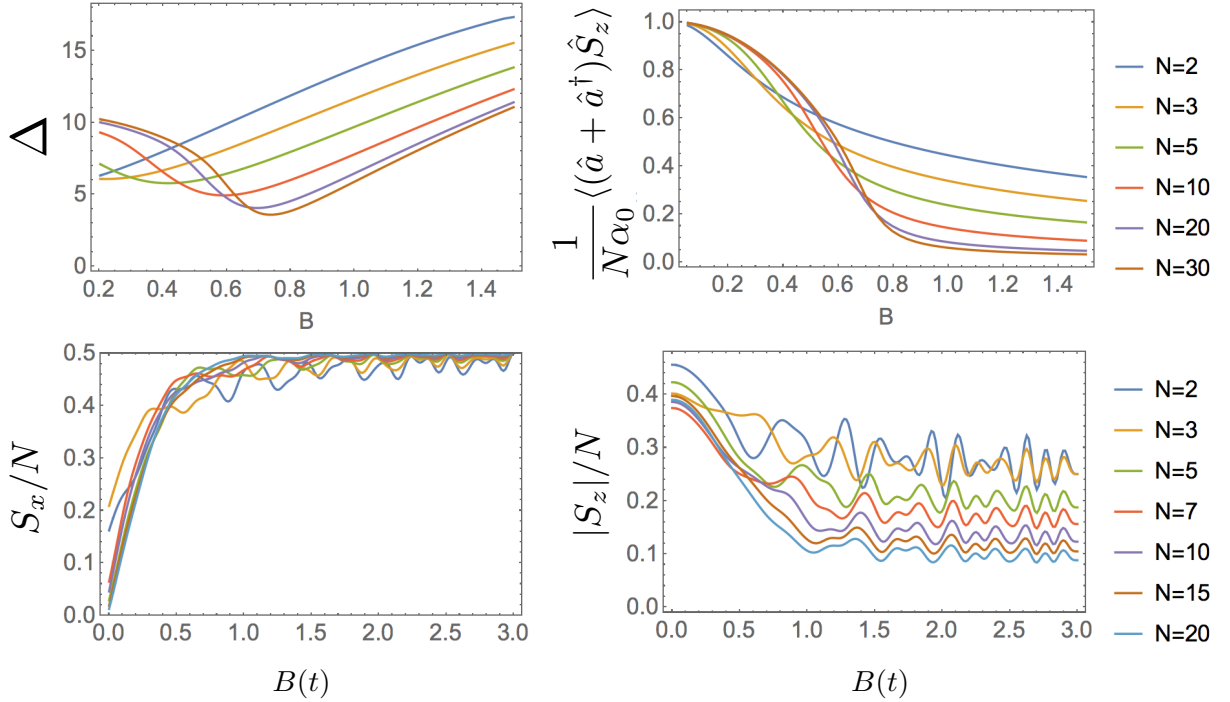* These two authors contributed equally

FIG. 1. Key quantities and observables of Dicke model as a function of atom number N and transverse field B. Energy gap Δ is between the ground-state and excited state in the same parity sector. Magnetization $|S_z|$ and mean spin projection S_x are computed for a LIN ramp with $t = 2$ms and other parameters taken as per Fig. 2b of the manuscript.
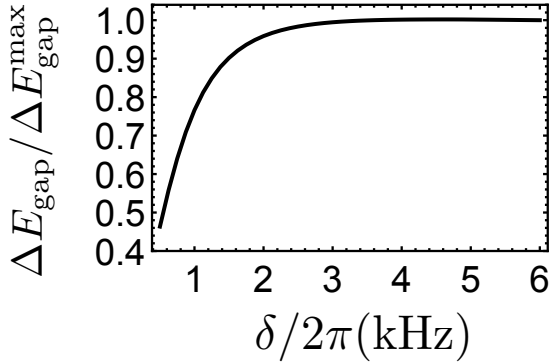

FIG. 2. The size of the gap as a function of the detuning from the COM for $N = 40$. As the size of the detuning increases, the resonant region of the Dicke model moves away from the quantum critical point separating the normal and superradiant phases. The energy gap at the critical point eventually saturates to a maximum value $\Delta E_{\text{gap}}^{\text{max}}$.

The choice of the sign in the superposition state Eq. (1) is dictated by the spin-phonon parity symmetry of the Dicke Hamiltonian. Specifically, $\hat{H}$ is preserved under the simultaneous transformation of $\hat{S}_z \to -\hat{S}_z$, $\hat{S}_y \to -\hat{S}_y$ and $\hat{a} \to -\hat{a}$, and the associated conserved quantity of the Hamiltonian is the generator of the symmetry $\hat{\Pi} \equiv e^{i\pi(\hat{a}^\dagger \hat{a} + \hat{S}_x + \frac{N}{2})}$. This symmetry dictates that when ramping from high to low field, the state $|\psi_{0,N/2}^{Nor}\rangle$ will adiabatically connect to the superposition $|\psi_{0,N/2}^{S}\rangle$, to conserve the parity $\langle \hat{\Pi} \rangle = e^{i\pi N}$. Specifically, for even N the ground-state will be the symmetric superposition with $\langle \hat{\Pi} \rangle = 1$, whilst for odd N the ground-state is the anti-symmetric superposition with $\langle \hat{\Pi} \rangle = -1$. Without loss of generality, we assume for the following that N is even and thus we fix the sign of the superposition to be positive.

Since the spin and phonon degrees of freedom are entangled in the ground-state [Eq. (1)], the state obtained by tracing over the phonon degree of freedom is characterized by the reduced density operator

$$\hat{\rho}_s = \frac{1}{2}\left[|N/2\rangle_z\langle N/2|_z + |-N/2\rangle_z\langle -N/2|_z\right]$$
$$+ \frac{e^{-|\alpha_0|^2}}{2}\left[|-N/2\rangle_z\langle N/2|_z + |N/2\rangle_z\langle -N/2|_z\right].$$

As the displacement amplitude $|\alpha_0|$ is increased, the reduced density matrix exponentially loses any information about the coherences which are exhibited in the spin-phonon superposition state. As a concrete example, the ground-states of the main text typically have a mean phonon occupation $|\alpha_0|^2 \sim 2$–30 depending on the chosen parameters (i.e., detuning and spin-phonon coupling), leading to $e^{-|\alpha_0|^2} \lesssim 0.1$. To fully probe the available coherences via only the spin degree of freedom, we must first transform Eq. (1) to a spin and phonon

product state,

$$|\psi_{\mathrm{SB}}\rangle = |\phi\rangle \otimes \frac{1}{\sqrt{2}}\Big(|N/2\rangle_z + |-N/2\rangle_z\Big), \qquad (2)$$

where $|\phi\rangle$ is some arbitrary state characterizing the phonon degree of freedom.

A possible procedure to achieve this decomposition is the following: At the conclusion of the ramp protocol, we fix the transverse field at $B = 0$ and quench the detuning $\delta \to \delta' = 2\delta$. The spin-phonon state is then allowed to evolve for a duration $t_d = \pi/\delta'$. In the interaction picture, the initial spin-phonon superposition state evolves as

$$|\psi_{\mathrm{SB}}\rangle = \hat{U}(t)|\psi^S_{0,N/2}\rangle, \qquad (3)$$

where

$$\hat{U}(t) = \hat{U}_{SB}(t)\hat{U}_{SS}(t), \qquad (4)$$

$$\hat{U}_{\mathrm{SS}}(t) = \exp\left(-i\frac{J}{N}\hat{S}_z^2 t\right), \qquad (5)$$

$$\hat{U}_{\mathrm{SB}}(t) = \hat{D}(\beta(t,\delta')S_z). \qquad (6)$$

Here, $\hat{U}(t)$ is the propagator corresponding to the Dicke Hamiltonian with $B = 0$ [Eq. 1 of the main text]. The propagator is comprised of two parts, the spin-spin propagator $\hat{U}_{\mathrm{SS}}(t)$ and the spin-phonon propagator $\hat{U}_{\mathrm{SP}}(t)$ where $\beta(t,\delta) = -g_0(1 - e^{-i\delta t})/(2\delta\sqrt{N})$ (see [3] for a more detailed discussion).

If at the end of the ramp we quench the detuning to $\delta' = 2\delta$ and apply $\hat{U}(t)$ for $t_d = \pi/\delta'$, such that $\beta(t_d, \delta') = -gN/(2\delta)$, it is then clear that $\hat{U}_{SB}$ will displace the phonon coherent states (in a direction dependent on the sign of the S_z component) back to vacuum, $|\pm\alpha_0, 0\rangle \to |0\rangle$. We illustrate this displacement in Fig. 3. Note that the action of $\hat{U}_{SS}$ on the spin component of the ground-state imprints an irrelevant global phase $\varphi = JN t_d/2$ on the decoupled state Eq. (2).

An alternative, but closely related, procedure to disentangle the spin-phonon state is to drive the spin-phonon coupling on resonance, $\delta \to \delta' = 0$. In this case, one must shift the phase of the drive by $\pi/2$ such that the spin-phonon coupling transforms as $\frac{g_0}{\sqrt{N}}(\hat{a} + \hat{a}^\dagger)\hat{S}_z \to \frac{ig_0}{\sqrt{N}}(\hat{a} - \hat{a}^\dagger)\hat{S}_z$, and subsequently evolve the system for a duration $t_d = 1/|\delta|$. Following this procedure results in a spin-dependent coherent displacement of the phonon state back to vacuum, $|\pm\alpha_0, 0\rangle \to |0\rangle$, in a manner similar to the previously discussed protocol.

We make one further point regarding the disentangling protocols. In the experimental system we generally characterize the initial state of the phonons as a thermal ensemble $\hat{\rho}_{\bar{n}}$ while the spin-degree of freedom is prepared in a pure state, such that the initial spin-phonon state is $\hat{\rho}_{SB}(0) = \hat{\rho}_{\bar{n}} \otimes |-N/2\rangle_x\langle -N/2|_x$. If the protocol is adiabatic and there is no coupling between the excited energy levels, then not only is the ground-state component of this initial ensemble mapped to the weak-field
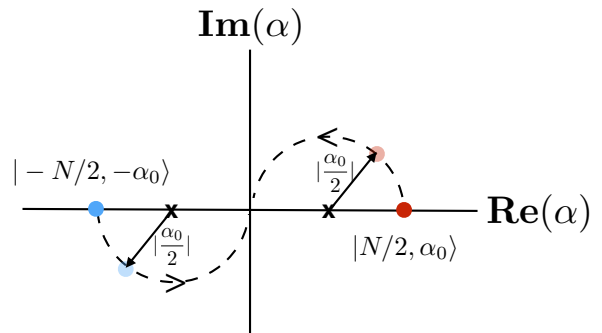

FIG. 3. Schematic of the disentangling protocol to extract a pure spin cat-state from the spin-phonon ground-state $|\psi^S_{0,N/2}\rangle$. At the end of the ramp, we quench the detuning $\delta \to 2\delta$ and evolve the system for an additional duration $t_d = \pi/|2\delta|$ at fixed $B = 0$. The phonon states start at opposing coherent amplitudes and undergo a spin-dependent coherent displacement which maps them to the phonon vacuum state.

ground-state of the Dicke Hamiltonian, but the excited fraction due to the thermal distribution is also mapped identically. This implies that the final state at the end of the ramp protocol will be a mixture of the true ground-state and the low-lying excitations, which, if $\delta^2 < g^2 N$, can be characterised as displaced Fock states $|\pm\alpha_0, n\rangle$ where n corresponds to the number of phonon excitations above the true ground-state.

The action of this protocol on these states is to identically displace the phonon state such that $|\pm\alpha_0, n\rangle \to |n\rangle$. This maps the spin-phonon excited states to the form of a product state identical to Eq. (2). Hence, tracing the phonons out of these excited states also recovers the spin cat-state.

IV. QUALITATIVE EFFECTS OF INITIAL PHONON OCCUPATION

In the main text we comment that the oscillations in the spin observable $\langle|\hat{S}_z|\rangle$ at short times is an indication of a non-negligible initial thermal occupation of the phonon mode (Fig. 2 of main text). Here, we support this conclusion by comparing results of theoretical calculations with different initial phonon occupation. Taking relevant parameters as per Fig. 2 of the main text and considering only the EXP ramp for simplicity, we plot the theoretical results for evolution of $\langle|\hat{S}_z|\rangle$ in Fig. 4. We observe that if the phonons are taken to be initially in a vacuum state, the short time dynamics displays only extremely weak signs of oscillations. In contrast, when the phonons are taken to be initially described by a thermal ensemble with mean occupation $\bar{n} = 3\text{-}9$ there are signficant oscillations at short-times, consistent with the observed experimental data. Moreover, the final magnetization at the conclusion of the ramp protocol is much
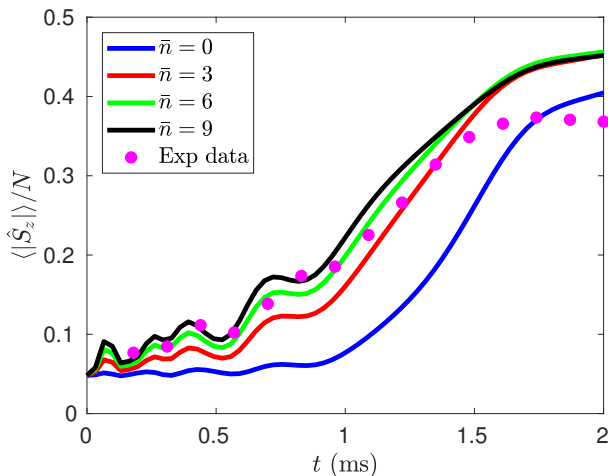
FIG. 4. Comparison of magnetization $\langle |\hat{S}_z| \rangle$ from experimental data and theoretical calculations for different initial thermal occupation $\langle \hat{a}^\dagger \hat{a} \rangle = \bar{n}$ of the phonon mode. The amplitude of the oscillations at $t \lesssim 1$ clearly increase with $\bar{n}$, whilst the frequency appears to remain comparitively fixed. Data is for an EXP ramp, with all other parameters taken as per Fig. 2b of the manuscript.

larger than that predicted from the vacuum case. The various values of $\bar{n}$ plotted give relatively similar agreement with the experimental data. However, $\bar{n} = 6$ is chosen in the main text as this is consistent with the estimated limit from Doppler cooling in the experiment.

V. INFERENCE OF SPIN-PHONON CORRELATIONS

As detailed in the main text, we infer the presence of spin-phonon correlations from the time evolution of the spin observable $\langle \hat{S}_x \rangle$. Specifically, starting from the Lindblad master equation for the density matrix of the spin-phonon system $\hat{\rho}$,

$$\frac{d\hat{\rho}}{dt} = -\frac{i}{\hbar} \left[\hat{H}^{\mathrm{Dicke}}, \hat{\rho} \right] + \frac{\Gamma_{el}}{2} \sum_{i=1}^{N} \left(\hat{\sigma}_i^z \hat{\rho} \hat{\sigma}_i^z - \hat{\rho} \right), \quad (7)$$

wherein we have assumed single-particle dephasing is the dominant decoherence mechanism, it then follows that

$$\frac{d\langle \hat{S}_x \rangle}{dt} = \frac{g_0}{\sqrt{N}} \langle \left(\hat{a} + \hat{a}^\dagger \right) \hat{S}_y \rangle - \Gamma_{el} \langle \hat{S}_x \rangle. \quad (8)$$

From here it is straightforward to rearrange for the relation between the spin-phonon correlation and the evolution of $\langle \hat{S}_x \rangle$:

$$\mathcal{C}_{\mathrm{sp-ph}} \equiv \langle \left(\hat{a} + \hat{a}^\dagger \right) \hat{S}_y \rangle = \frac{\sqrt{N}}{g_0} \left(\Gamma_{el} \langle \hat{S}_x \rangle + \frac{d\langle \hat{S}_x \rangle}{dt} \right). \quad (9)$$

We emphasize that evaluation of this spin-phonon correlation directly from either ground-state $|\psi_{0,N/2}^{\mathrm{Nor}} \rangle$

$|\psi_{0,N/2}^{S} \rangle$ yields $\mathcal{C}_{\mathrm{sp-ph}} = 0$, and this result has been confirmed numerically for all transverse field strengths B for the systems considered in the main text. This directly implies that the finite value reported in the main text is due to contributions from excited states. Such contributions may come from diabatic excitations created throughout the ramping protocol or from the initial thermal phonon ensemble.

In the main text, we extract the spin-phonon correlation from the experimental data using the RHS of Eq. (9) and evaluating the time-derivative numerically with a one-sided derivative. We model dephasing using $\langle \hat{S}_x \rangle_\Gamma = \langle \hat{S}_x \rangle_{\Gamma=0} e^{-\Gamma t}$ in our theoretical calculations, and extract the theoretically predicted spin-phonon correlation in an identical manner.

VI. EXPERIMENTAL OPTIMISATION OF RAMP PROTOCOLS

To experimentally optimize the ramp protocols demonstrated in this work, we chose to optimize with respect to the total magnetization $\langle |\hat{S}_z| \rangle$ at the end of the ramp. For the EXP ramp, we compared approximately 20 different ramp profiles that utilized different exponential decay rates. Specifically, we would perform an experiment where the effective transverse field was ramped from the initial field $B(t = 0)$ at a fixed decay rate to $B \approx 0$, where we then measured the spin-projection M_z^{exp} along the $\hat{z}$-axis. This experiment was repeated, typically $500 - 700$ times, to gather statistics on the resulting distribution and obtain a measurement of $\langle |\hat{S}_z| \rangle$ from the histogram of M_z^{exp} measurements. We then picked a ramp profile with a different exponential decay rate, and repeated this procedure. After identifying the exponential decay rate that optimized the final magnetization $\langle |\hat{S}_z| \rangle$, we performed experiments that measured the magnetization distribution $P(M_z^{\mathrm{exp}})$ when stopping the ramp at different times, as discussed in the main text.

When performing these ramp sequences and observing the distributions of M_z^{exp}, in some cases the distributions would be biased to positive or negative spin-projection. This can be observed in the distribution of Fig. 5(a) at zero offset frequency. Such an effect can be explained by a small longitudinal magnetic field that breaks the symmetry of the ground state. The small longitudinal field was likely due to imperfect nulling of the Stark shift from the off-resonant laser beams that generate the spin-dependent force [4]. We would observe that this effect varies day to day. To compensate for this effect, during the ramp we would apply a small frequency offset to the microwaves that provided the effective transverse field. For each frequency offset, we would measure the distribution of measurements M_z^{exp} at the end of the transverse field ramp as shown in Fig. 5(a). For the appropriate offset, the distribution would be balanced, with large, separated peaks at positive and negative values of M_z^{exp}. To choose the optimum, we plot $\langle \hat{S}_z \rangle$ as a function of the

a)
Spin Distribution
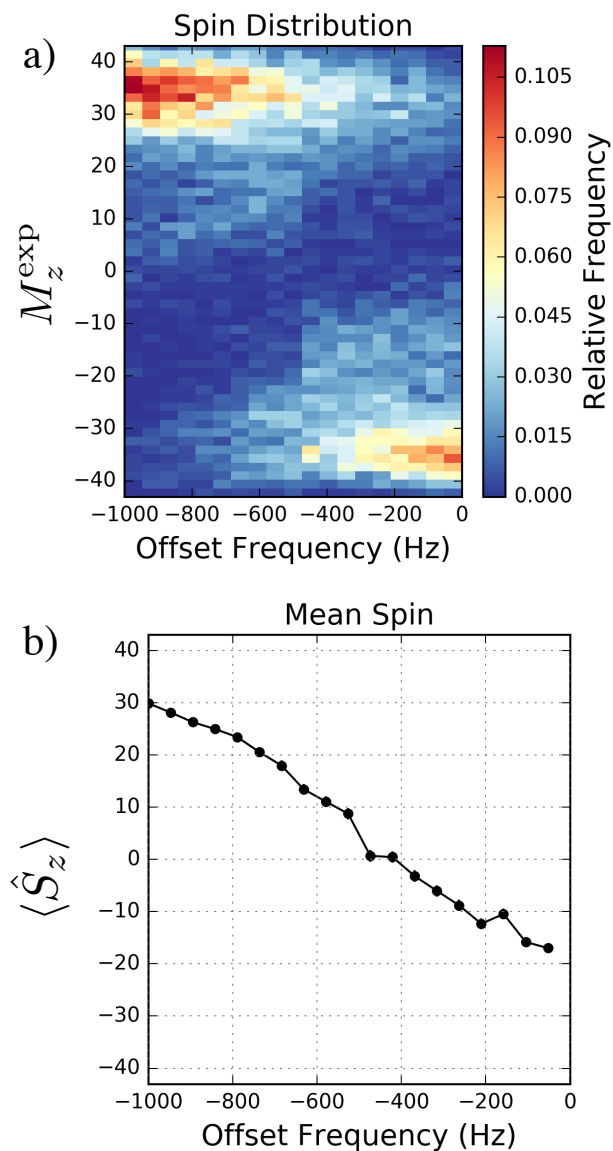
frequency offset and extract the zero crossing, as shown in Fig. 5(b).

b)
Mean Spin

FIG. 5. Balancing the $P(M_z^{\mathrm{exp}})$ distributions. (a) $P(M_z^{\mathrm{exp}})$ distribution functions extracted from experimental measurements of the spin-projection M_z^{exp} at the end of an EXP ramp of the transverse magnetic field to zero. The distribution functions are plotted as a function of frequency offset of the microwaves that generate the effective transverse magnetic field from the spin-flip resonance in the absence of the spin-dependent force. (b) Plot of the average magnetization $\langle \hat{S}_z \rangle$ from (a) as a function of the microwave offset frequency. An offset frequency that balanced the distributions at the end of the ramping sequence, defined by $\langle \hat{S}_z \rangle$, was used in studies described in the main text that measured the spin-projection distribution when stopping the ramp at different times.

[1] C. Emary and T. Brandes, Phys. Rev. Lett. **90**, 044101 (2003).

[2] C. Emary and T. Brandes, Phys. Rev. E **67**, 066203 (2003).

[3] M. L. Wall, A. Safavi-Naini, and A. M. Rey, Phys. Rev. A **95**, 013602 (2017).

[4] J. G. Bohnet, B. C. Sawyer, J. W. Britton, M. L. Wall, A. M. Rey, M. Foss-Feig, and J. J. Bollinger, Science **352**,

1297 (2016).